# The complex high-mass star-forming region IRAS 15507-5359

P. Persi,[1]★ M. Tapia,[2]★ M. Roth,[3,4] D. Elia[1] and J. A. López-Vázquez[5,6]

[1]*INAF–Istituto Astrofisica e Planetologia Spaziale, Via Fosso del Cavaliere 100, I-00133 Roma, Italy*

[2]*Instituto de Astronomía, Universidad Nacional Autónoma de México, Ensenada, B. C., CP 22830, Mexico*

[3]*Las Campanas Observatory, Carnegie Institution of Washington, La Serena, Chile*

[4]*Giant Magellan Telescope Organization, Pasadena, CA 91107, USA*

[5]*Instituto de Radioastronomía y Astrofísica, Universidad Nacional Autónoma de México, Morelia, Mich., CP 58089, Mexico*

[6]*Facultad de Ingeniería, Universidad Autónoma de Chihuahua, Chih, Mexico*

## ABSTRACT

The far-infrared IRAS 15507-5359 source is known to be a medium-mass star-forming region associated with a compact H II region and a near-infrared embedded cluster. We present a survey of infrared-calibrated images ranging from 1.2 to 500 μm obtained with the Baade telescope at Las Campanas Observatory, and the *Herschel* space telescope with additional archive *Spitzer* data. We confirm the distance to the complex to be 5.0 kpc. Three *Herschel* far-infrared sources are found, I, II, III, identified with dense cores at different evolutionary stages. One (III) is a starless infrared dark cloud showing, near its edge, two infrared reflection nebulae (R1) and (R2) with dispersed young stellar populations, including a knot of shocked $H_2$ line emission. Both show considerable polycyclic aromatic hydrocarbon emission. Core II has associated a radio H II region and a deeply embedded one-million-year-old cluster (Cl 1) that contains more than 45 young stellar objects, reddened by at least 20 visual magnitudes. About 20 per cent of them show considerable infrared excess emission. Core I appears void of a near-infrared population, and coincides with a long emission bar that resembles a photodissociation front. We determine the properties of the two most luminous Class I sources in the region by fitting models of young stars with accreting discs and envelopes to their 1–500 μm spectral energy distributions. This is another example of a medium-mass region with at least three well-defined active centres of star formation separated by about 1 pc and at different evolutionary stages.

**Key words:** circumstellar matter – stars: formation – infrared: stars.

## 1 INTRODUCTION

As reported by several authors, understanding the processes that result in the formation of massive stars (O, B-stars with masses $\geq 8\,M_\odot$) is quite complex and requires good observational knowledge about star-forming environments. This is well illustrated in a recent article by Tapia et al. (2014) which reports a detailed study of the complex massive star-forming region RCW 121 (IRAS 17149-3916) using sub-arcsec resolution near-infrared (near-IR) images, *Spitzer* and *Herschel* data. A similar analysis of the region associated with IRAS 15507-5359 is presented here.

Based on *IRAS* colours, IRAS 15507-5359 has been classified by Palla et al. (1991) as a *high* source, meaning that it is most probably a massive stellar object at a very early evolutionary state. An ultra-compact HII (UCH II) region has been detected at 6 cm (3.9 GHz; Caswell & Haynes 1987) and at 18 and 22 GHz (Sánchez-Monge et al. 2013) close to this *IRAS* source. An embedded young stellar cluster was found to be associated with the UCH II region by

Dutra et al. (2003) using data from the Two Micron All Sky Survey (2MASS) survey. CS(2–1) line emission has also been detected in this area by Bronfman, Nyman & May (1996), and the presence of two 1.2 mm continuum emission clumps was reported by Beltrán et al. (2006). No methanol maser source at 44 GHz and at 6.7 GHz was detected in surveys by Slysh et al. (1994) and Walsh et al. (1997). The kinematic distances to this complex are 5.0 and 9.0 kpc, though Sánchez-Monge et al. (2013) chose the 'near' distance (5.0 kpc) based on the H I line absorption method (cf. Green & McClure-Griffiths 2011).

We obtained new sub-arcsec resolution near-IR broad-band and narrow-band images centred close to the nominal position of the *IRAS* source. These observations are compared with *Herschel* images obtained from the Herschel Infrared GALactic plane survey (Hi-GAL; Molinari et al. 2010) and are described in Section 2. In addition, archive Infrared Array Camera (IRAC)/*Spitzer* images are used to supplement these observations.

Using photometry from these images, spectral energy distributions (SEDs) were constructed for the most luminous sources. Their properties, and those of the associated stellar population are discussed in Section 3. The conclusions are listed in Section 4.

★ E-mail: paolo.persi@iaps.inaf.it (PP); mt@astrosen.unam.mx (MT)

## 2.2 Near-infrared images and photometry

Near-IR images, through standard broad-band *JHKs* filters as well as through narrow-band $H_2$ ($\lambda_o = 2.125\,\mu m$, $\Delta\lambda = 0.024\,\mu m$) and Br $\gamma$ ($\lambda_o = 2.165\,\mu m$, $\Delta\lambda = 0.022\,\mu m$) filters, were collected on the night of 2009 June 10 using the Perssons Auxiliary Nasmyth Infrared Camera (PANIC) attached to the Magellan Baade 6.5 m telescope at Las Campanas Observatory (Chile). PANIC uses a Hawaii 1024 × 1024 HgCdTe array that provides a 120 arcsec × 120 arcsec field of view with a scale of 0.125 arcsec pixel$^{-1}$ (Martini et al. 2004). We obtained nine dithered frames, each of 60, 40 and 20 s effective integration time in $J$, $H$, $K_s$, respectively, and 60 s in the narrow-band filters, by offsetting the telescope by 6 arcsec between consecutive exposures. The mean measured full width at half-maximum (FWHM) point spread function (PSF) in $K_s$ was $\simeq$0.5 arcsec. PSF-fitting photometry was performed using the DAOPHOT Stellar Photometry Package (Stetson, 1987) within the Image Reduction and Analysis Facility (IRAF) environment.[1] The photometry was calibrated using several standard stars each night from the extended list of faint standards of Persson et al. (1998)[2] for use with the Magellan telescopes.

Photometry of sources in the area under study that are brighter than 12.0 in $K_s$, saturated on PANIC, was taken from the 2MASS Point Source Catalogue (Skrutskie et al. 2006), and the final PSF photometry catalogue will be submitted to the Centre de Donnes Stellaires[3] (CDS) in machine-readable format.

A total of 814 stars with intrinsic photometric errors amounting to less than 15 per cent in both $H$ and $K$ were measured; of these, 657 were also measured in $J$. From the brightness distribution of the detected sources in each broad-band filter, we defined the approximate completeness limiting magnitude of the PSF-photometry survey to be that for which the number of field sources ceases to increase monotonically (cf. Tapia et al. 2009). These values were $J = 18.5$, $H = 17.6$ and $K_s = 17.3$. However, many fainter stars were also measured and included in the sample.

Fig. 2 shows two composite colour near-IR images of the studied region. The left-hand panel illustrates the image obtained by combining the $J$ (blue), $H$ (green) and $K_s$ (red) individual frames. The colour image presented in the right-hand panel was constructed from the $K_s$ broad-band frame (blue) and the narrow-band images centred in Br $\gamma$ (green) and the $H_2$ (red) lines.

The $JHK_s$ image reveals a number of red ($K$-band-dominated) nebulosities. The largest and brightest nebula lies in direction of core II and two other fainter, roundish and smaller nebulae lie in the north and north-east outskirts of core III. Finally, a long, filamentary red nebula oriented NW–SE lies in the direction of core I. On top of these, an evenly distributed population of blue ($J$-band-dominated) field stars is evident, while a large number of faint, much redder stars appear distributed inhomogeneously. The latter are discussed in Section 3.3, where the properties of the stellar population are analysed. It is important to stress that the two extremely bright (in the near-IR) stars just north-west of the centre of the observed field have near-IR colours that imply late-type giant or supergiant photospheres, most likely unrelated to the star-forming region.
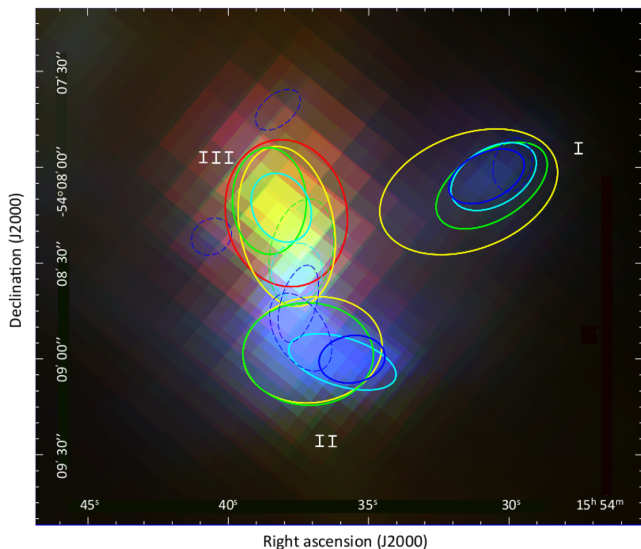


**Figure 1.** *Herschel* composite colour image constructed from 70 μm (blue), 250 μm (green) and 500 μm (red) images. The *Herschel* sources detected at 70, 160, 250, 350 and 500 μm are represented with blue, cyan, green, yellow, red ellipses, respectively. The size and position angle of the ellipses are those evaluated by CUTEX at half-height of the two-dimensional Gaussian fitted to the source brightness profile at each band. Three clumps, labelled I, II and III, are detected in at least three adjacent bands in the 160–500 μm range, making it possible to fit a modified blackbody to their SEDs. Counterparts at different wavelengths of these clumps are represented with solid ellipses, while other detections and detections at 70 μm in general, are represented with dashed ellipses.

## 2 OBSERVATIONS

### 2.1 Hi-GAL images and photometry

As part of the *Herschel* Hi-GAL survey, we obtained 70, 160, 250, 350 and 500 μm calibrated images of IRAS 15507-5359. Source extraction and photometry was done using the Curvature Threshold Extractor package (CUTEX; Molinari et al. 2011) independently at each band. Subsequently, band merging was carried out based on simple spatial association criteria, as in Elia et al. (2013). The methods for reduction and analyses used are described by Tapia et al. (2014). Fig. 1 illustrates the *Herschel* three-colour image of an area of 2 arcmin × 2 arcmin around the *IRAS* position. This is composed from the 70 (blue), 250 (green) and 500 μm (red) frames. Ellipses are overplotted to indicate the position, size and inclination of the various Hi-GAL sources present in this area as extracted by CUTEX. One can appreciate how strongly the morphology of the emission varies with wavelength and inherent spatial resolution, making it difficult to correctly build SEDs over a large spectral range. Even if counterparts are detected at several wavelengths, the occurrence of multiplicity (especially at 70 μm) can lead to inaccuracies in SED building. We resolved such cases following Elia et al. (2013): when a source at $\lambda_2$ has multiple counterparts at $\lambda_1$, with $\lambda_1 < \lambda_2$, only the $\lambda_1$ counterpart closest to the centroid at $\lambda_2$ is matched. In this respect, three main sources or clumps with a complete and regular SEDs, here named IRAS 15507-I, II and III, have been found. Their fluxes are reported in Table 1. As shown in Fig. 1, cores I and II dominate the 70 μm emission, while core III is not detected at this wavelength but its emission extends to longer wavelengths (350 and 500 μm) and has also been detected at 1.2 mm by Beltrán et al. (2006; their clump 2).

---

[1] IRAF is distributed by the National Optical Astronomy Observatory, which is operated by the Association of Universities for Research in Astronomy, Inc. under contract to the National Science Foundation.
[2] http://www.lco.cl/telescopes-information/magellan/instruments/panic/panic-online-documentation/panic-manual/new-ir-standards-for-panic/
[3] http://cdsarc.u-strasbg.fr/mnras

**Table 1.** Flux densities of the three *Herschel* cores detected in IRAS 15507-5359.

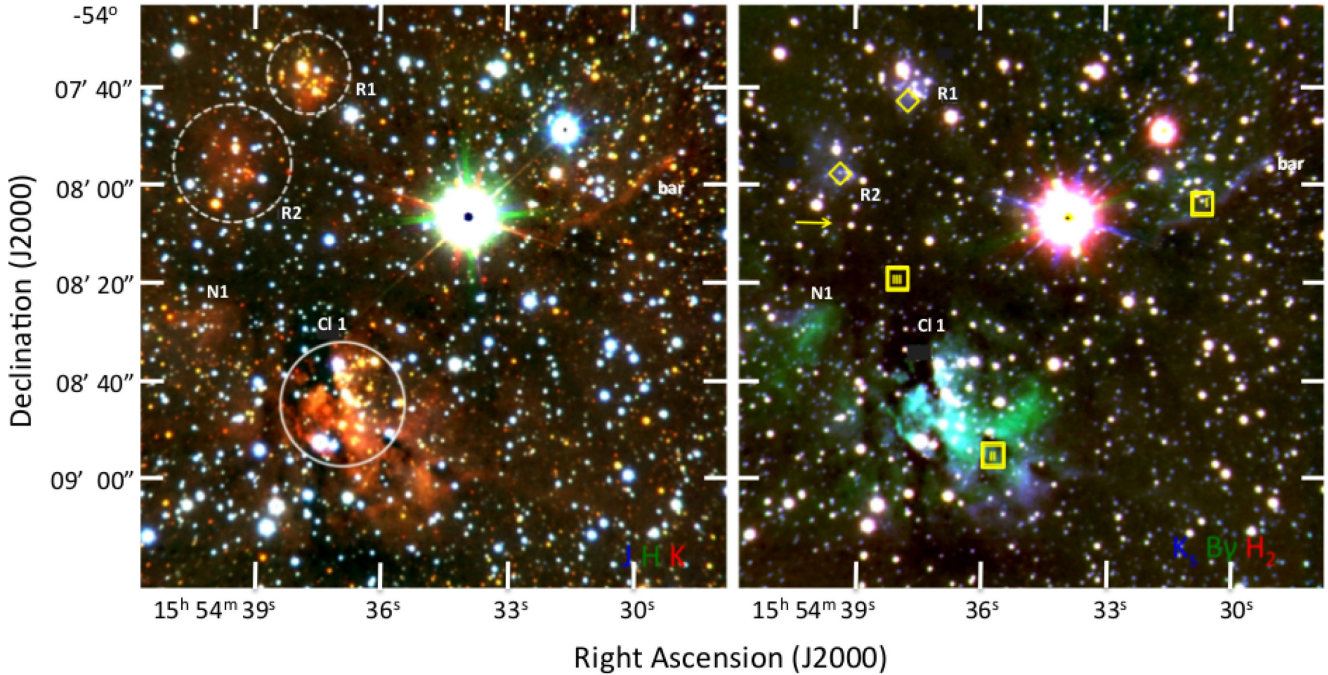| Source | $\alpha$(2000)<br>(h m s) | $\delta$(2000)<br>(° ′ ″) | F[160]<br>(Jy) | F[250]<br>(Jy) | F[350]<br>(Jy) | F[500]<br>(Jy) |
|---|---|---|---|---|---|---|
| IRAS 15507-I | 15 54 30.8 | −54 08 03 | 84.3 ± 2.9 | 36.4 ± 1.7 | 14.2 ± 4.3 | − |
| IRAS 15507-II | 15 54 35.6 | −54 08 57 | 189.5 ± 31.9 | 198.7 ± 11.7 | 66.7 ± 20.0 | − |
| IRAS 15507-III | 15 54 37.5 | −54 08 18 | 144.6 ± 20.8 | 166.5 ± 4.0 | 107.3 ± 3.0 | 48.0 ± 2.2 |



**Figure 2.** Left-hand panel: $JHK_s$ (blue, green, red) image of a region around IRAS 15507-5359. The circles represent the positions and sizes of the embedded cluster, Cl 1 and the near-IR reflection nebulae R1 and R2 that are discussed in Section 3.3. Right-hand panel: colour image constructed with the $K_s$ (blue), Br $\gamma$ (green) and $H_2$ (red) individual images. The yellow-labelled squares mark the centres of the dense cores I, II and III; the rhombuses mark the 70 μm emission peaks associated with the reflection nebulae, and the arrow points to the position of the single $H_2$ 2.12 μm emission knot.

The nature of the nebulous emission can be derived from the $K_s$Br $\gamma$$H_2$ image (Fig. 2, right-hand panel). There, the green extended features are dominated by emission of the ionized hydrogen 2.17 μm Br $\gamma$ line, thus delineating H II regions; the blue ones are dominated by continuum stellar light scattered by dust particles, and the red features indicate regions where the molecular hydrogen 2.12 μm emission dominates. The presence of an IR-bright asymmetrical H II region close to the position of core II is evident, with a faint extension to the east. This corresponds to the radio H II region G327.759-0.351, 0.56 pc in diameter, that is ionized by a UV flux equivalent to that emitted by an O7 ZAMS star (Sánchez-Monge et al. 2013). As will be discussed in detail in Section 3.3.1, this H II region is associated with an embedded IR cluster, here named Cl 1. We find that some scattered light is also present, implying dust particles that are mixed with the ionized gas. Two small reflection nebulae, labelled R1 and R2 in Fig. 2, are located to the north of core III. They shine mostly from dust-scattered light and present only faint traces of ionized gas emission. Additionally, a very faint 'bar' is seen in the 2.2 μm continuum, $H_2$ and Br $\gamma$ emission centred at the position of core I. Finally, a single, small (<2 arcsec) knot of 2.12 μm $H_2$ emission is located at the edge of the reflection nebula R2. Note that none of these features are seen on any published optical image of the field, implying large amounts of dust extinction. These morphological features are marked in Fig. 2.

In order to have a more complete census of the deeply embedded population associated with the nebular regions, we performed 3 arcsec aperture photometry of additional 36 point sources up to 2 mag fainter than the PSF photometry limits, and which lie within the boundaries of the nebulae Cl 1, R1 and R2. These additional data will be referred to as 'aperture photometry'.

### 2.3 *Spitzer* GLIMPSE archive images and photometry

Flux-calibrated images of the IRAS 15507-5359 region from the *Spitzer* Galactic Legacy Infrared Midplane Survey Extraordinaire (GLIMPSE; Benjamin et al. 2003; Churchwell et al. 2009) key program survey taken at 3.6, 4.5, 5.8 and 8 μm with the IRAC (Fazio et al. 2004) on board the *Spitzer* Space Telescope (Werner et al. 2004) were retrieved from the public image archive. A colour composite image made up of the IRAC 3.6, 4.5 and 8 μm frames of the surveyed area is presented in Fig. 3. Point-source extraction and aperture (3 arcsec) photometry was performed of the point-like sources on the calibrated images with DAOPHOT. The sky value for each source was measured on a ring of radius 4 arcsec and width 2 arcsec after filtering for source contamination. Final calibration was made by comparing the fluxes with those of isolated stars in the field from the GLIMPSEII catalogue. A total of 32 sources could be measured photometrically with intrinsic errors smaller than 0.25 mag in both IRAC channels 1 and 2 frames (3.6 and 4.5 μm).
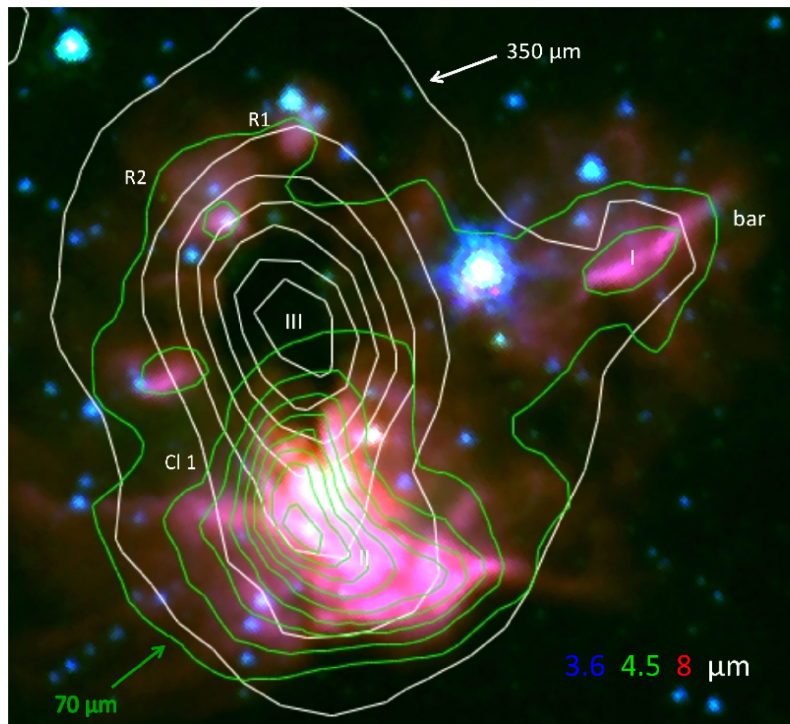
**Figure 3.** Composite colour image constructed with the IRAC 3.6 μm (blue), 4.5 μm (green) and 8 μm (red) individual images. The green contours are the 70 μm and the white contours the 350 μm *Herschel* emissions. The red pixel and the blue diffraction ring and spikes around the brightest stellar source are artefacts. The size of the image is 2.4 arcmin × 2.2 arcmin and it is centred at $\alpha(2000) = 15^h54^m35\overset{s}{.}6$, $\delta(2000) = -54°08'24''$. North is to the top, east to the left.

Note that the IRAC images are shallower and have much lower spatial resolutions than those from PANIC, explaining the rather small number of mid-IR counterparts. Furthermore, the extended emission, dominated by polycyclic aromatic hydrocarbon (PAH) particles, especially within the H II region G327.759-0.351, preclude the photometric detection of a number of stellar sources embedded in it. We were able to perform reliable 3.6, 4.5, 5.8 μm photometry for only 20 IRAC point sources with near-IR counterparts, and only a few of them could be measured also at 8 μm. These data are presented in Table 2.

## 3 DISCUSSION

### 3.1 Properties of the massive dense cores

In the observed field we recognized three bright far-IR sources detected in at least three consecutive bands in the 160–500 μm range. The emission in the 70 μm band, in contrast, more likely results from warmer material rather than the cold dust component traced at the longer wavelengths. We used the latter to define the presence of three dense cores, named I, II and III, following, e.g. Schneider et al. (2012) and Elia et al. (2013).

From the observed *Herschel* flux densities $F_\nu$ reported in Table 1, we built the SEDs of the three aforementioned clumps (Fig. 4). To compensate for flux excesses typically found at the SPIRE longest wavelengths (Motte et al. 2010; Giannini et al. 2012; Elia et al. 2013), at 350 and 500 μm we adopted the flux-scaling strategy followed by these authors. Also, for core III we included the 1.2 mm flux density value given by Beltrán et al. (2006) in the SED.

We derived masses and temperatures of the clumps by fitting single-temperature modified black bodies to their SEDs following

Giannini et al. (2012) and Elia et al. (2013). For a distance of 5.0 kpc (Section 3.2), the SED fits are shown in Fig. 4, and the corresponding masses and temperatures for the three cores in the IRAS 15507-5359 region are listed in Table 3.

### 3.2 Distance estimate

The available kinematic distances to the radio H II region and molecular cloud associated with IRAS 15507-5359 are 5.0 (near) and 9.0 (far) kpc (Sánchez-Monge et al. 2013). The present *JHK* photometry of all sources indicates that nearly 90 per cent of the stars in the $(J − H)$ versus $(H − K)$ diagram (shown in the left-hand panel of Fig. 5) lie on the 'normal' reddening vector (Rieke & Lebofsky 1985) for late-type stars with extinction corresponding to $A_V \leq 7$, or $A_K \leq 0.8$. Given the presence of a large, dense molecular cloud associated with the IRAS 15507-5359 complex, the obvious interpretation is that the bulk of these lowly reddened stars lie in the foreground and that the total Galactic interstellar extinction up to where IRAS 15507-5359 is located is $A_K = 0.8$, corresponding to $A_V = 7.0$ for a 'normal' extinction law. Using the 2MASS All Sky Survey catalogue, Marshall et al. (2006) modelled empirically the Galactic interstellar extinction in three dimensions based on $A_K$ measurements for a large range of galactic coordinates $(l, b)$ combined with Besançon's model of the Galaxy (Robin et al. 2003). One of the reference directions in Marshall et al.'s study was $l = 325$ and $b = 0°$, which happens to be the direction to IRAS 15507-5359 (its precise galactic coordinates are $l = 328°$ and $b = 0°3$). Their $A_K$ versus $d$ plot (see fig. 13 of Marshall et al. 2006) indicates that in that direction, $A_K = 0.8$ of Galactic dust extinction corresponds to a distance of between 4.5 and 5.5 kpc. The mean is the previously determined 'near' kinematic value. We therefore conclude that the

**Table 2.** Coordinates and magnitudes of sources measured in three IRAC channels or large IR excesses.

| α̃ (2000) (h m s) | δ (° ′ ″) | J (mag) | H (mag) | K (mag) | [3.6] (mag) | [4.5] (mag) | [5.8] (mag) | [8] (mag) | Notes |
|---|---|---|---|---|---|---|---|---|---|
| 15 54 31.0 | −54 08 06 | – | – | – | 10.90 ± 0.20 | 10.80 ± 0.20 | 8.30 ± 0.20 | – | core I, t4 |
| 15 54 31.6 | −54 07 47 | 9.84 ± 0.02 | 9.20 ± 0.02 | 9.01 ± 0.02 | 9.08 ± 0.01 | 8.94 ± 0.02 | 8.81 ± 0.03 | – | field star |
| 15 54 33.5 | −54 08 18 | – | 19.60 ± 0.19 | 15.13 ± 0.02 | 11.55 ± 0.12 | 10.29 ± 0.05 | 9.32 ± 0.17 | 8.97 ± 0.45 | |
| 15 54 33.9 | −54 08 05 | 8.14 ± 0.02 | 6.48 ± 0.04 | 5.70 ± 0.02 | 5.12 ± 0.01 | 5.24 ± 0.01 | 4.94 ± 0.01 | 4.61 ± 0.02 | field star |
| 15 54 35.5 | −54 08 44 | 18.55 ± 0.02 | 14.65 ± 0.01 | 12.50 ± 0.01 | 11.00 ± 0.04 | 11.01 ± 0.11 | 9.30 ± 0.15 | – | PAH, Cl 1 |
| 15 54 36.2 | −54 08 35 | 16.36 ± 0.01 | 13.97 ± 0.01 | 12.50 ± 0.01 | 10.89 ± 0.06 | 9.57 ± 0.03 | 7.92 ± 0.03 | 5.91 ± 0.03 | Cl 1 |
| 15 54 36.2 | −54 08 27 | – | 17.31 ± 0.01 | 14.49 ± 0.04 | 12.35 ± 0.16 | 11.12 ± 0.09 | 9.84 ± 0.29 | – | Cl 1 |
| 15 54 36.3 | −54 08 41 | 19.19 ± 0.02 | 16.02 ± 0.12 | 13.98 ± 0.02 | 11.71 ± 0.24 | 11.01 ± 0.24 | – | – | Cl 1 |
| 15 54 36.5 | −54 08 36 | 18.79 ± 0.03 | 15.12 ± 0.02 | 13.02 ± 0.03 | 11.06 ± 0.08 | 10.03 ± 0.07 | – | – | Cl 1 |
| 15 54 36.7 | −54 07 43 | – | 17.31 ± 0.01 | 14.49 ± 0.04 | 10.91 ± 0.03 | 10.84 ± 0.04 | 9.38 ± 0.08 | – | PAH |
| 15 54 36.9 | −54 08 42 | 15.31 ± 0.01 | 13.47 ± 0.01 | 12.41 ± 0.02 | 11.13 ± 0.13 | 9.56 ± 0.08 | 7.63 ± 0.17 | 5.56 ± 0.16 | Cl 1 |
| 15 54 36.9 | −54 08 49 | 17.34 ± 0.01 | 14.59 ± 0.01 | 13.09 ± 0.01 | 12.07 ± 0.20 | 11.38 ± 0.20 | – | – | Cl 1 |
| 15 54 37.0 | −54 08 36 | 13.37 ± 0.03 | 12.96 ± 0.08 | 12.47 ± 0.08 | 11.11 ± 0.14 | 10.48 ± 0.15 | 8.13 ± 0.14 | – | Cl 1, t5 |
| 15 54 37.1 | −54 08 07 | – | >21.1 | 17.20 ± 0.10 | 12.02 ± 0.08 | 11.13 ± 0.06 | 10.00 ± 0.17 | – | SW of R2 |
| 15 54 37.1 | −54 08 32 | – | 18.9 ± 0.1 | 15.28 ± 0.09 | 11.13 ± 0.06 | – | – | – | Cl 1 |
| 15 54 37.2 | −54 07 36 | – | 16.92 ± 0.03 | 14.10 ± 0.04 | 10.69 ± 0.03 | 9.93 ± 0.03 | 8.14 ± 0.08 | – | R1 |
| 15 54 37.3 | −54 08 46 | – | 17.77 ± 0.12 | 15.87 ± 0.02 | 11.22 ± 0.15 | 10.02 ± 0.10 | 7.00 ± 0.20 | 5.27 ± 0.07 | core II, t3 |
| 15 54 37.5 | −54 07 39 | 17.57 ± 0.01 | 15.13 ± 0.02 | 13.63 ± 0.03 | 11.68 ± 0.2 | 10.39 ± 0.2 | – | – | R1 |
| 15 54 37.5 | −54 07 39 | – | 16.71 ± 0.02 | 14.81 ± 0.03 | 11.28 ± 0.2 | 10.47 ± 0.2 | – | – | R1, t2 |
| 15 54 37.8 | −54 07 34 | 15.68 ± 0.01 | 13.18 ± 0.02 | 11.32 ± 0.03 | 9.32 ± 0.02 | 8.58 ± 0.02 | 7.65 ± 0.04 | 6.55 ± 0.07 | R1 |
| 15 54 38.0 | −54 08 38 | – | >21.1 | 16.20 ± 0.03 | 11.45 ± 0.12 | 10.70 ± 0.15 | 7.76 ± 0.20 | 6.10 ± 0.07 | Cl 1 |
| 15 54 38.2 | −54 07 55 | – | 20.00 ± 0.11 | 15.32 ± 0.12 | 12.04 ± 0.07 | 11.17 ± 0.06 | 9.54 ± 0.12 | – | R2 |
| 15 54 38.3 | −54 08 45 | – | 19.4 ± 0.1 | 15.88 ± 0.05 | 11.45 ± 0.08 | 10.90 ± 0.15 | 8.60 ± 0.20 | – | Cl 1 |
| 15 54 38.5 | −54 09 05 | 12.84 ± 0.03 | 11.52 ± 0.02 | 11.02 ± 0.02 | 10.48 ± 0.03 | 10.44 ± 0.04 | 8.68 ± 0.08 | 7.34 ± 0.10 | PAH |
| 15 54 38.6 | −54 09 07 | 17.43 ± 0.02 | 14.75 ± 0.01 | 13.40 ± 0.02 | 12.25 ± 0.20 | 11.96 ± 0.20 | – | – | NE of R1 |
| 15 54 39.1 | −54 07 56 | – | 17.30 ± 0.12 | 14.44 ± 0.08 | 10.84 ± 0.07 | 10.07 ± 0.05 | 7.84 ± 0.06 | 6.28 ± 0.07 | R2, t1 |
| 15 54 39.4 | −54 07 50 | 17.04 ± 0.02 | 14.49 ± 0.02 | 13.03 ± 0.02 | 11.50 ± 0.05 | 10.85 ± 0.05 | – | – | R2 |
| 15 54 39.9 | −54 08 02 | 17.53 ± 0.02 | 14.06 ± 0.01 | 12.04 ± 0.01 | 10.71 ± 0.03 | 10.42 ± 0.04 | 10.45 ± 0.34 | – | R2 |
| 15 54 40.7 | −54 08 01 | – | 17.13 ± 0.01 | 14.81 ± 0.02 | 12.82 ± 0.10 | 12.17 ± 0.08 | – | – | R2 |
| 15 54 41.0 | −54 08 26 | – | 17.23 ± 0.01 | 13.72 ± 0.02 | 10.66 ± 0.03 | 10.41 ± 0.04 | – | – | N1 |

*Notes.* t1: three stars in IRAC beam, *HK* refer to the sum; t2: two stars in IRAC beam, *HK* refer to the sum; t3: Cl 1, extended *HK* emission (diam. =1.4 arcsec); t4: PAHs 'bar'; faint *H − K* = 2.6 point source displaced 1.1 arcsec from PAH peak; t5: near-IR star embedded in PAH nebulosity.
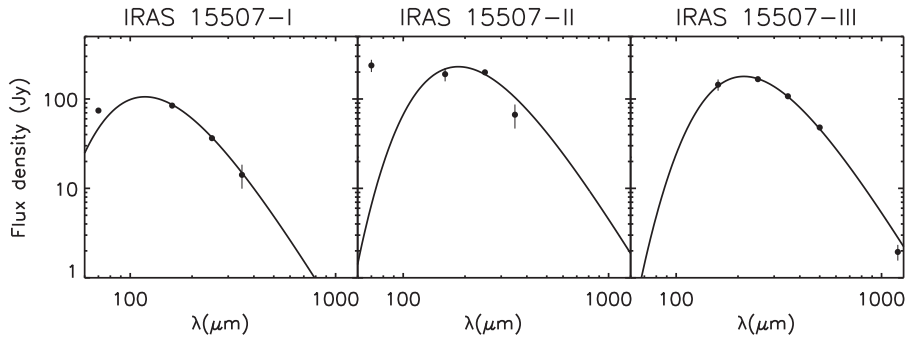


**Figure 4.** SEDs of the three cores observed with *Herschel*. The continuous lines are the best-fitting modified black bodies described in Section 3.1. The flux at 70 μm is plotted but was not considered for the fit.

confirmed distance to IRAS 15507-5359 is around $d = 5.0$ kpc, a value which we adopt for this work.

## 3.3 The young stellar population

When the large number of 'blue' foreground stars in the $JHK_s$ Baade image field is ignored, three areas with large projected overdensities of faint red stars become apparent. This effect could be caused by inhomogeneous extinction, which is apparent in the region, and/or by the presence of real clustering of stars. The statistical photometric properties of the source population do provide enough information to differentiate between these two possibilities. A map of the

**Table 3.** Masses and temperatures of the dense cores in IRAS 15507-5359.

| Source | M (M⊙) | T$_d$ (K) |
|---|---|---|
| IRAS 15507-I | 160 | 24.9 |
| IRAS 15507-II | 3063 | 16.4 |
| IRAS 15507-III | 3953 | 15.6 |

distribution of all the 849 stars measured (PSF and aperture photometry) in the $H$ and $K$ bands in the area surveyed (2 arcmin × 2 arcmin) is presented in Fig. 6. We divided the stars into two categories depending on their $J − H$ and $H − K$ colour indices: the
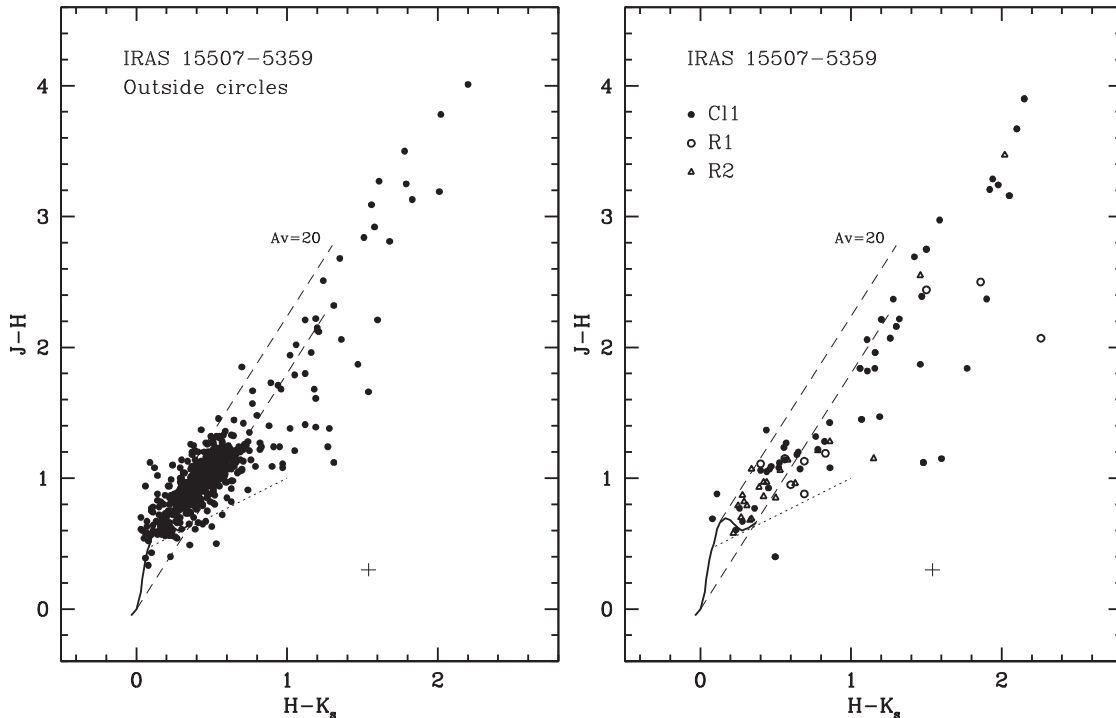
**Figure 5.** $J - H$ versus $H - K_s$ diagram of all sources measured in $JHK_s$ with uncertainties ≤0.15 in each filter. Photometry of sources that saturate on the PANIC frames was taken from the 2MASS catalogue. The right-hand panel is for sources within the circular boundaries of Cl 1 (filled circles), R1 (open circles) and R2 (open triangles) of radii 12.8 arcsec, 8.5 arcsec, 12.0 arcsec, respectively (see Table 4). The left-hand panel shows the sources outside those circles (filled circles). In both panels, the solid lines mark the locus of main-sequence (Koornneef 1983) stars, the dashed lines delineate the reddening band for all main-sequence and giant stars (Rieke & Lebofsky 1985). The dotted line indicates the locus occupied by the Classical T Tauri stars. The small crosses near the lower-right corner show the maximum formal errors.

first is comprised by very red stars with $(H - K_s) > 1$ together with those stars with $JHK$ colours that imply significant $K$-band excess emission. The latter stars are those having colour indices $(H - K_s)$ at least 0.2 mag larger than those expected for OB-type photospheres with the observed $(J - H)$ colour and normal extinction. These IR-excess stars are naturally interpreted to be young stars with discs and are plotted as filled circles in Fig. 6. The rest of the sources, with colours indicative of them being field (foreground and background) stars, comprise the second category and are represented in Fig. 6 by small crosses.

The $K$-band source distribution, even when only sources with PSF photometry are considered, indicates that the IR-excess stars are preferentially compressed in three areas: (1) One corresponds to a previously catalogued cluster (Cl 1) of embedded young stars (Dutra et al. 2003) clearly associated with the radio H II region G327.759-0.351 (Sánchez-Monge et al. 2013); (2) a compact stellar group of faint red stars immersed in the red reflection nebula R1 and (3) a larger, more dispersed, group of stars embedded in the reflection nebula R2. Both R1 and R2 are seen projected on the north-east edge of the very dense core III. Table 4 lists the main results of the source (with and without IR excesses) counts in Cl 1, R1 and R2 together with their measured projected size, assuming a circular geometry.

Fig. 5 presents two $(J - H)$ versus $(H - K_s)$ plots of the sources measured in these three photometric bands. The right-hand panel is for sources located within the boundaries of Cl 1, R1 and R2, as specified in Table 4, whereas the left-hand panel includes all sources in the surveyed area outside these circles. The contrast in photometric properties between these populations is evident. Outside the circles, 91 per cent of the 597 sources measured in $JHK$

occupy the locus of late-type stars reddened by $A_V \leq 7.0$. As discussed in Section 3.2, they are interpreted as being foreground stars, while another 4 per cent have colours of highly reddened $8 < A_V < 32$ late-type photospheres, assumed to belong to the background, and only 3 per cent show near-IR excesses. The fraction of foreground and background late-type stars in Cl 1 was only 55 per cent, 33 per cent in R1 and 77 per cent in R2.

Similarly, $K_s$ versus $H - K_s$ plots were constructed for all 813 sources measured in these colours and shown in Fig. 7. The left-hand panel is for 724 sources outside Cl 1, R1 and R2 and the right-hand panel is for the 47 sources belonging to Cl 1, 19 to R1, 24 to R2 and 1 on the 'bar'. For the near-IR sources with mid-IR point-like counterparts that could be measured in 3.6 and 4.5 μm, we present the $H - K_s$ versus $K_s - [3.6]$ diagram in Fig. 8, and in Fig. 9 we present the [3.6]–[4.5] versus [4.5]–[5.8] plot, when the last colour index could be determined. The analyses of the two-colour and colour–magnitude diagrams will be discussed in detail in the following subsections.

### 3.3.1 The UCH II region G327.759-0.351 and its embedded cluster Cl 1 associated with IRAS 15507-II

G327.759-0.351 is the large, bright H II region that dominates the diffuse emission in the $K$ band (red in left-hand panel of Fig. 2) and in the Br $\gamma$ line (green in the right-hand panel of Fig. 2). No trace of this nebulosity is seen on the red Digital Sky Survey images. Based on their radio-continuum fluxes at 18.0 and 22.8 GHz, Sánchez-Monge et al. (2013) determined the physical parameters of the UCH II region: mass of ionized gas $M_{H II} = 4.5\,M_\odot$ and
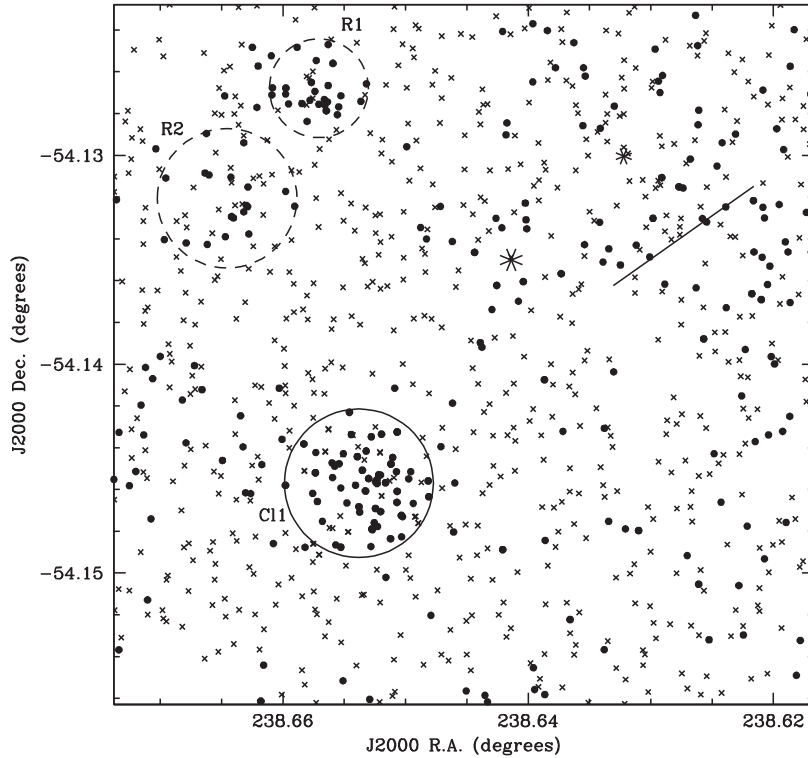
**Figure 6.** Spatial distribution of all sources with PSF photometry in *H* and *K* in the whole 2 arcmin × 2 arcmin Baade field, with the addition of deeper aperture photometry within regions Cl 1, R1 and R2. The filled circles represent stars that have colour indices $H - K \geq 1$ or show significant *JHK* excess, while the crosses (x) represent the rest of the stars. The continuous line circle of radius 12.8 arcsec marks the observed boundaries of the embedded cluster Cl 1; the dashed line circles represent the locations of the near-IR reflection nebulae R1 and R2. The continuous straight line represents the Br $\gamma$ and H$_2$ 'bar' associated with core I. The large asterisks mark the positions of the two brightest late-type field stars in the surveyed area.

**Table 4.** Observed statistics from *H* and *K* bands source counts in embedded cluster Cl 1, within reflection nebulae R1, R2 and surroundings.

| Area | Coordinates of centre $\alpha(2000)$ (h m s) | $\delta$ (° ′ ″) | Radius (arcsec) | Number of sources | Projected density (arcmin$^{-2}$) | Fraction of stars $H - K_s \geq 0.8$ or NIR excess | Projected density[†] $H - K_s < 0.8$ (arcmin$^{-2}$) | Notes |
|---|---|---|---|---|---|---|---|---|
| Cl 1 | 15 54 36.91 | −54 08 44.5 | 12.8 | 47 | 329 | 57% | 98 | PSF only |
| R1 | 15 54 37.70 | −54 07 36.4 | 8.5 | 19 | 302 | 68% | 47 | PSF only |
| R2 | 15 54 39.50 | −54 07 55.4 | 12.0 | 24 | 191 | 17% | 134 | PSF only |
| Out* | | | | 723 | 197 | 21% | 149 | PSF only |
| Cl 1 | 15 54 36.91 | −54 08 44.5 | 12.8 | 63 | 441 | 68% | – | incl. ap. phot. |
| R1 | 15 54 37.70 | −54 07 36.4 | 8.5 | 30 | 476 | 73% | – | incl. ap. phot. |
| R2 | 15 54 39.50 | −54 07 55.4 | 12.0 | 32 | 254 | 34% | – | incl. ap. phot. |

*Notes.* *Surveyed area excluding circles Cl 1, R1 and R2 (3.67 arcmin$^2$); [†]Stars measured in *J*, *H* and $K_s$.

log $N$(Ly) = 48.61 (O7 ZAMS), with a radius of 0.28 pc (for $d$ = 5 kpc). The ionization can only be provided by members of the embedded young cluster, as discussed previously. As our near-IR photometry is more than three magnitudes deeper than 2MASS, we managed to determine accurately the extent of the embedded cluster by performing simple radial *K*-band source counts, as described at the end of this section (see Tapia et al. 2014). The IR cluster was found to be contained within a radius of 12.8 arcsec, which corresponds to 0.31 pc (for $d$ = 5 kpc). Baade and *Spitzer*/IRAC close-up colour-coded images of this region are presented in Fig. 10. They evince a complex structure of the gas and dust as well as in the distribution of the cluster members. We note that the filamentary PAH-dominated (pink) emission in the 3.6 and 8 μm IRAC channels closely follows the distribution of the (red) *K*-band diffuse emission, dominated by the Br $\gamma$ line (see also right-hand panel of Fig. 2),

a common feature in young H II regions. In contrast, we note that in Sánchez-Monge et al.'s (2013) radio-continuum maps, although barely resolved, the bright radio free–free gas emission appears round, implying the presence of intervening dense dust cloudlets that absorb heavily the H II region emission in the near- and mid-IR. The warm and cool dust forming these clouds emit thermally in the far-IR, giving rise to the complex morphology seen in the low-resolution *Herschel* images, as can be seen in Figs 1 and 3. The warm dust giving rise to the 70 μm emission appears to have a different morphology from the emission at $\lambda \geq 150$ μm, which traces the cooler dust, all within a single molecular core that we named core II (Tables 1 and 2).

Close to the dense core II and the centre of the radio H II region, a bright and very red mid-IR source, named IRAS 15507-II, stands out on the IRAC images for having the reddest colours and
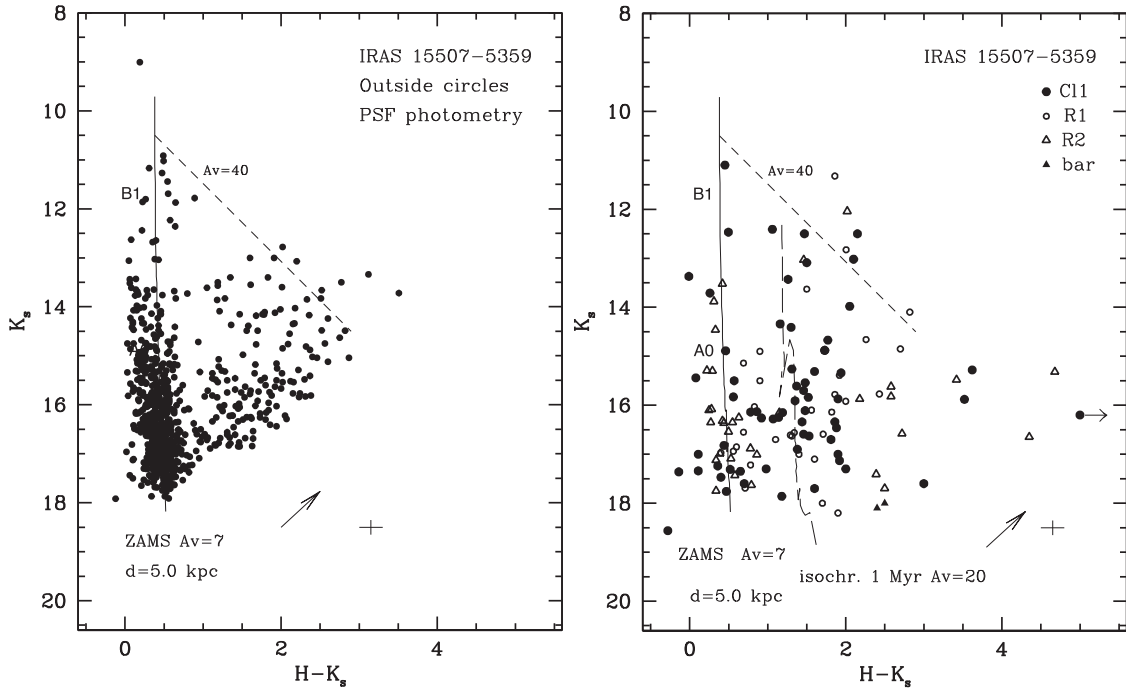
**Figure 7.** $K_s$ versus $H - K_s$ diagram of sources measured in $H$ and $K_s$ with uncertainties $\leq 0.15$ in each filter. Photometry of sources that saturate are taken from the 2MASS catalogue. The right-hand panel is for sources inside the Cl 1, R1 and R2 circles (see text) and the left-hand panel shows the sources outside those circles. For reference, the almost vertical solid line delineates the ZAMS for $d = 5.0$ kpc and $A_V = 7$. The short-dashed line is the reddening vector of length $A_V = 40$. In the right-hand panel, the long-dashed line represents the 1 Myr isochrone (Siess et al. 2000) for the same distance and $A_V = 20$. The arrow represents the average slope of the near-IR emission excess caused by discs around YSOs, as determined by López-Chico & Salas (2007). The small cross near the lower-right corner shows the maximum formal error for each colour.
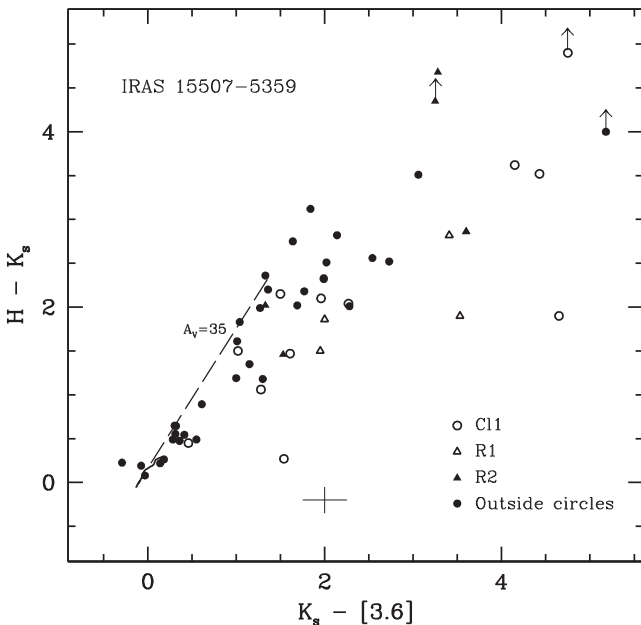


**Figure 8.** $H - K_s$ versus $K_s - [3.6]$ diagram of all sources measured in $H$, $K_s$ and the 3.6 µm IRAC band with uncertainties <0.25 in each filter. Different symbols are used for stars inside circles Cl 1, R1 and R2 and those lying outside them. The solid line marks the locus of the main sequence (Koornneef 1983) and the dashed line shows the reddening vector (Rieke & Lebofsky 1985). The small cross near the bottom of the plot illustrates the maximum formal error for each colour.
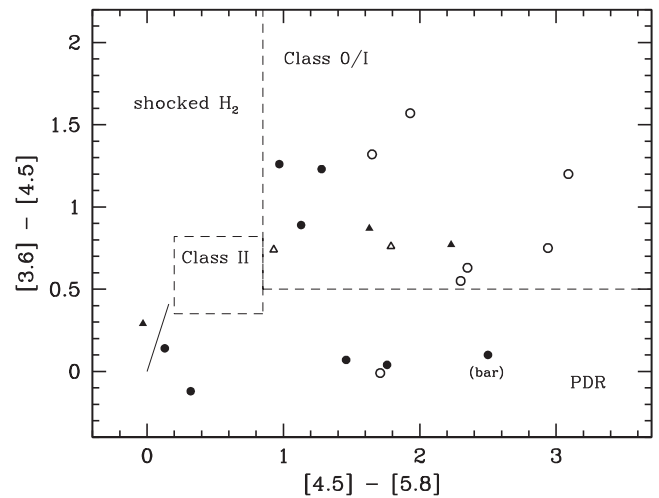


**Figure 9.** [3.6]–[4.5] versus [4.5]–[5.8] diagram of all sources measured in the three IRAC bands. The symbols used for sources in and outside regions Cl 1, R1 and R2 are the same as in Fig. 8. The dashed rectangles mark the locii of the Class II and Class 0/I sources and the labels 'shocked H₂' and 'PDR' mark, respectively, the areas occupied by shocked regions emitting molecular hydrogen lines and PAH-emission-dominated photodissociation regions (Ybarra et al. 2014). The continuous line is the reddening vector (Flaherty et al. 2007).

being the brightest at $\lambda > 4$ µm (see Table 2). Its coordinates are $\alpha(2000) = 15^h54^m37^s.3$, $\delta(2000) = -54°08'45''$. This source is marked with a long arrow in Fig. 10. Although unresolved in the low spatial resolution Spitzer images ($\geq 1.6$ arcsec), it is clearly resolved in all Baade images (1.3 to 2.2 µm), being centrally peaked with a
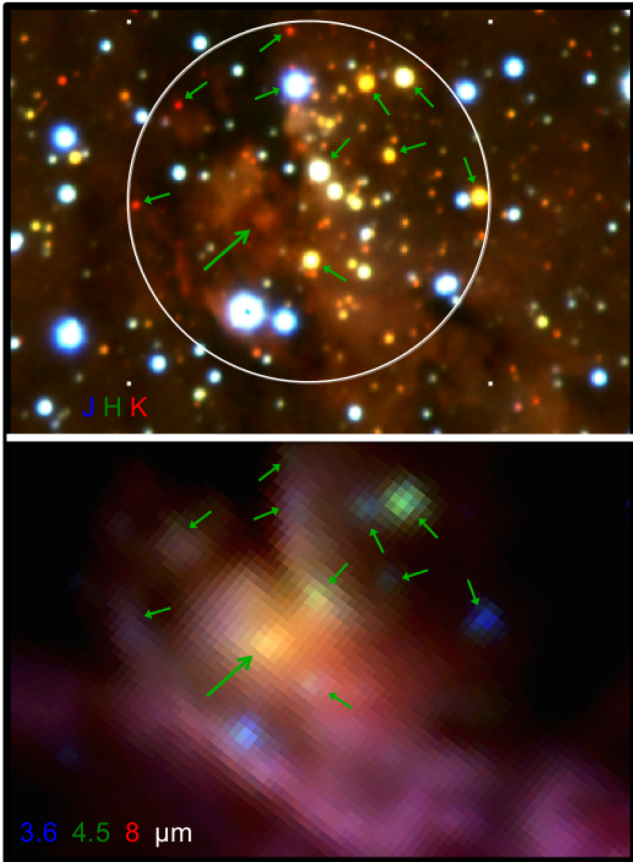
**Figure 10.** Close-up of the composite colour images of the cluster and radio H II region associated with core IRAS 15507-II. The upper panel shows the *J*, *H*, *K_s* image. The radius of the white circle representing the boundaries of the young embedded cluster is 12.8 arcsec. The lower panel is the IRAC 3.6, 4.5 and 5.8 µm image on the same scale. The centre of both panels is at $\alpha(2000) = 15^h54^m36^s\!.9$, $\delta(2000) = -54°08'46''$. The sources marked with green arrows, listed in Table 2, show large IR excesses. The brightest of these sources in the mid-IR, IRAS 15507-II, is indicated with a long arrow. Colour coding as in Fig. 13.

circular shape of diameter (FWHM) ∼1.4 arcsec (0.04 pc), almost three times larger than the seeing measured for the surrounding stars (FWHM = 0.5 arcsec). The narrow-band images in the Br γ and H₂ lines indicate that this small nebulous source has an emission nature of similar character to that of the rest of the H II region. Its location, very close to core II mapped in the far-IR by *Herschel*, suggests that this is the dominant, most luminous young stellar object (YSO), responsible for heating the dust in the core, as well as providing a good fraction of the UV photons that ionize the gas. Combining its near-IR, IRAC and *Herschel* flux densities (Tables 1 and 2) and the 1.2 mm flux (Beltrán et al. 2006), we constructed the SED for this source, displayed in the right-hand panel of Fig. 11. We fitted these fluxes to the infalling envelope-disc-central source radiation transfer model by Robitaille et al. (2006) by using the on-line tool described in Robitaille et al. (2007). The ranges of best-fitting (lower $\chi^2$) parameters, maintaining a fixed distance of 5.0 kpc, are given in Table 5. The measured total luminosity of IRAS 15507-II (1–1200 µm) is in the range $3.4$–$5.8 \times 10^3\,\mathrm{L}_\odot$, corresponding to a B0–B1 ZAMS. The Lyman-continuum emission from this YSO falls short from that required to ionize an H II with a radio-continuum flux similar to that determined by Sánchez-Monge et al. (2013) for

G327.759-0.351. This Lyman-continuum excess problem has been encountered in a significant fraction of H II regions by Lumsden et al. (2013), Sánchez-Monge et al. (2013), Urquhart et al. (2013) and Cesaroni et al. (2015). These last authors presented a statistical analysis and suggested a number of possible causes that may explain this effect.

We determined the physical properties of the embedded cluster Cl 1 by analysing the near- and mid-IR two-colour and colour–magnitude diagrams. Consider first the sample with measured *JHK* magnitudes: it contains 53 stars, including both the PSF and the considerably deeper aperture photometry in the Cl 1 area. The size of the sample is determined by the relatively small number of stars brighter than the survey's limiting magnitude in *J*, in turn caused by the very large extinction (i.e. large $J - H$ colours). The resulting $J - H$ versus $H - K_s$ diagram is shown in the right-hand panel of Fig. 5.

For the sake of consistency, while comparing the projected star densities in the Cl 1 area and in the total area surveyed excluding the Cl 1 + R1 + R2 circles, we must consider only the smaller sample of stars for which PSF photometry could be performed in the three filters, thus avoiding any statistical bias. The measured projected densities of foreground stars (i.e. those with $H - K_s < 0.8$) for the various studied zones are listed in Table 4. Assuming that the foreground star density is determined by the amount of extinction in front of the IRAS 15507-5259 complex, then it is clear that the extinction towards Cl 1 is significantly higher than the mean extinction for the overall surveyed area. On the other hand, we were able to PSF-measure, in *JHK*, 11 highly reddened early-type stars ($A_V > 12$) and 4 with large *K*-band excess emission in Cl 1, well in excess of the 1 expected from the star surface density measured in the surrounding field. This implies that more than 15 young PSF-measured stars in Cl 1 are cluster members. If we add the extra aperture photometry, this number increases to 34 (i.e. 41 per cent) with significant *K*-band excesses.

The photometric sample that includes all the sources measured in the *H* and *K_s* filters is, clearly, more complete. The $K_s$ versus $H - K_s$ diagram in the right-hand panel of Fig. 7 shows 63 sources in Cl 1, represented by solid dots (PSF and aperture photometry). In the figure, we draw with a continuous line the zero-age main sequence (ZAMS) for a distance of 5.0 kpc and $A_V = 7$ (Section 3.2) and also a $10^6$ yr isochrone (Siess, Dufour & Forestini 2000) reddened by $A_V = 20$. The latter proved to fit reasonably well (within $\Delta(H - K) < 0.3$) to a large fraction of the non-foreground stars observed in Cl 1. In fact, this colour–magnitude diagram is extremely useful to discern probable cluster members and separate them from foreground stars. It is also very useful to infer some of the basic physical parameters of the cluster and their members.

We first note that 20 sources with $H - K_s < 0.8$ are extincted by $A_V < 8$ and, thus, are foreground stars, with the probable exception of the brightest two, whose photometry (including *J*) is consistent with them being B0–B2 main-sequence cluster-member stars with $A_V = 8$. Secondly, 41 per cent (26) of the sources in this sample lie on the $10^6$ yr isochrone with $A_V = 20$. A further 21 per cent (13), including the near-IR counterpart to IRAS 15507-II, lie on a similar sequence with an extra visual extinction of 10 mag and/or significant *K*-band excess originating in circumstellar discs. Furthermore, there are four other sources with $H - K_s \geq 3.0$, the most embedded cluster members. Again, the presence of discs around these stars is indicated by large 3.6 and 4.5 µm excess emission (see Fig. 9). The total number of cluster members here reported is 43, or 68 per cent of the sample. In Fig. 10 we marked the most significant excess sources, also listed in Table 2.
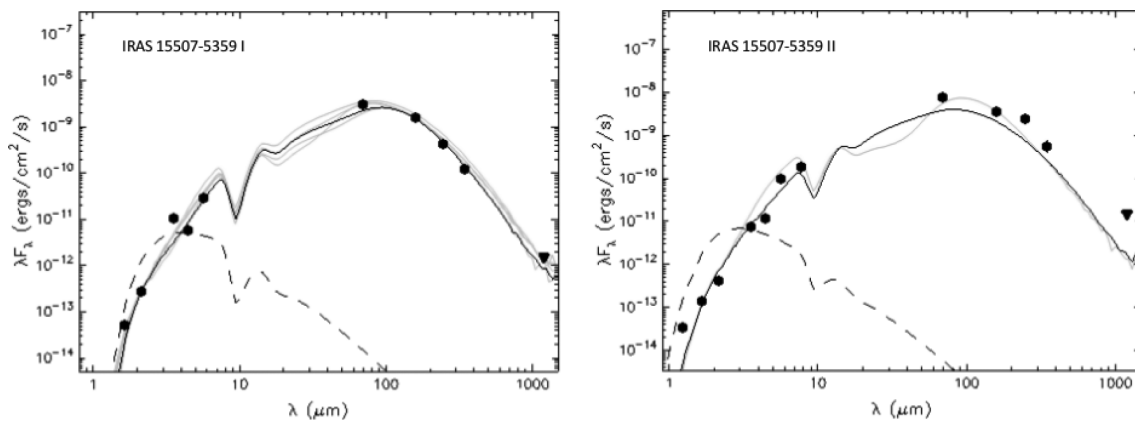
**Figure 11.** Left-hand panel: SED of source IRAS 15507-I. Right-hand panel: SED of source IRAS 15507-II. The best-fitting models of the SEDs derived from the Robitaille et al. (2007) fitting tool are overplotted. The range of parameters of the model fits for both sources are given in Table 5.

**Table 5.** Ranges of physical parameters for cores I and II from SED best fits using the Robitaille et al. (2007) tool.

| Parameters | Core I | Core II |
|---|---|---|
| Stellar mass ($M_\odot$) | 9.3–10.6 | 9.9–12.6 |
| Stellar temperature (K) | 5100–9200 | 9200–6630 |
| Envelope outer radius (au) | $3.4 \times 10^4$–$10.0 \times 10^4$ | $1.0 \times 10^5$–$2.8 \times 10^4$ |
| Envelope cavity angle (deg) | 4.3–10.3 | 9.2–5.9 |
| Env. accretion rate ($M_\odot$ yr$^{-1}$) | $1.8 \times 10^{-3}$–$3.7 \times 10^{-3}$ | $2.7 \times 10^{-3}$–$6 \times 10^{-3}$ |
| Disc mass ($M_\odot$) | $1.8 \times 10^{-3}$–$2.2 \times 10^{-1}$ | $1.8 \times 10^{-3}$–$4.6 \times 10^{-1}$ |
| Disc outer radius (au) | 29–76 | 73–112 |
| Disc accretion rate ($M_\odot$ yr$^{-1}$) | $2.12 \times 10^{-5}$–$3.1 \times 10^{-2}$ | $1.3 \times 10^{-8}$–$2.1 \times 10^{-2}$ |
| $A_V$ (mag) | 36–49 | 30–33 |
| $d$ (kpc) | 5.0 | 5.0 |
| $L_{bol}$ ($L_\odot$) | $2.1 \times 10^3$–$3.3 \times 10^3$ | $3.4 \times 10^3$–$5.8 \times 10^3$ |

The projected morphology of the cluster/H II region appears somewhat complicated by the highly inhomogeneous dust distribution in its surroundings. In spite of this, we assumed a spherical distribution while performing radial source counts in order to get a fair picture of the structure of the embedded cluster. For a series of rings with growing radii centred on $\alpha(2000) = 15^h54^m36^s91$, $\delta(2000) = -54°08'44''5$, we counted all stars that had $H - K$ indices smaller or larger than 0.8. Following the reasoning of the previous discussion, we assumed the former to be field stars and the latter to be cluster members, as these lie on the cluster isochrone with or without extra extinction or near-IR excess emission. The results are shown in Fig. 12. It is clear that the projected density distribution is not highly peaked, which is not surprising in such a dust-rich environment.

In summary, the diameter of the IRAS 15507 embedded cluster Cl 1 was determined to be 25.6 arcsec, or 0.62 pc, at a distance from the Sun of 5.0 kpc. It contains more than 45 stars down to a $K17.5$ corresponding to early-A ZAMS stars. Its age is around one million years and is reddened by $A_V = 20$–30 mag. The fraction of cluster members with excess emission in $K$ in our sample is around 20 per cent.

### 3.3.2 IRAS 15507-III and the stellar population in R1 and R2

This far-IR source is the most massive and coldest cloud in the region (Table 3). It was not detected in the PACS 70 μm band, while the 160–1200 μm SED (Fig. 4) is well fitted by our modified blackbody model (Section 3.1). A close look at the composite IRAC
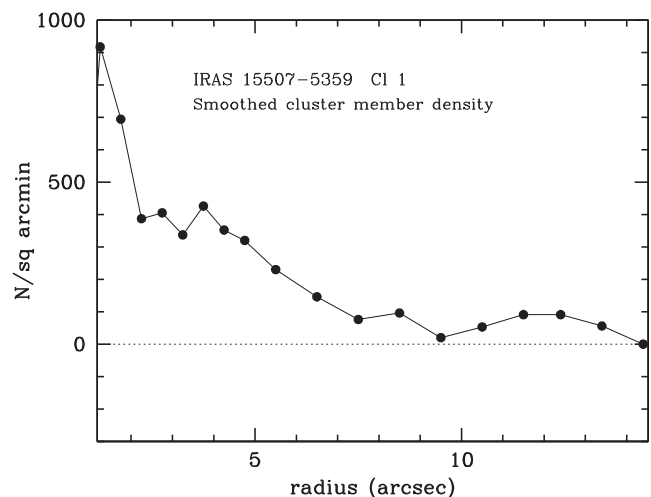


**Figure 12.** Smoothed projected radial distribution of the density of Cl 1 cluster members that lie on the 1 Myr isochrone in the $K_s$ versus $H - K_s$ diagram or having redder $H - K_s$ indices as described in Section 3.3.1. The coordinates of the centre of the cluster are given in Table 4.

and *Herschel* image shown in Fig. 3 evinces that the nucleus of the dense core, signposted by the peak far-IR emission IRAS 15507-III, corresponds to an IR dark cloud, as noted and catalogued by Peretto & Fuller (2009) in their *Spitzer* dark cloud catalogue (SDC327.768-0.344). In fact, only foreground stars are seen in that area in all our near- and mid-IR images. The cloud may still be collapsing and it
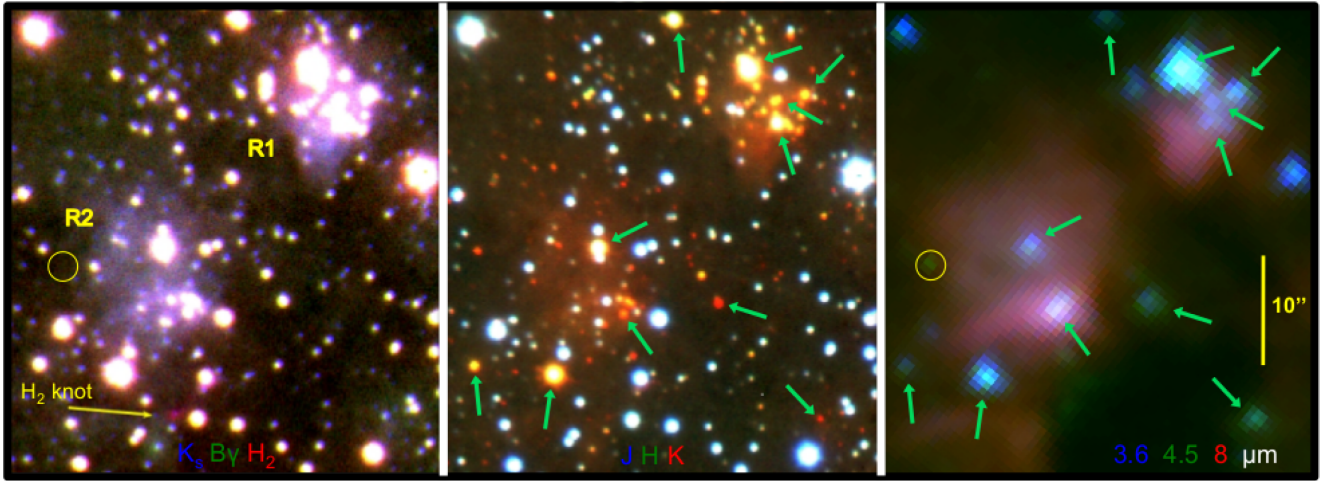
**Figure 13.** Close-ups of an area that includes the IR reflection nebulae R1 and R2 (Table 4) in the northeastern edge of the far-IR source IRAS 15507-III. The $K_s$, Br $\gamma$ and $H_2$ (red, green, blue) composite image is shown in the left-hand panel. Note the small $H_2$ emission knot, marked by a yellow arrow to the south of R2. The $JHK_s$ (red, green, blue) image is shown in the middle panel and the IRAC 3.6, 4.5 and 5.8 μm (red, green, blue) image is shown in the right-hand panel. The green arrows mark the stars with infrared excess listed in Table 2. The small yellow circle indicates the position of a 'IRAC green fuzzy knot' (see Section 3.3.2). All panels are on the same scale and centred at $\alpha(2000) = 15^h54^m38\overset{s}{.}8$, $\delta(2000) = -54°07'51''$. North is to the top, east to the left.

appears that the formation of stars has not yet started inside this (starless) dense cloud. Particularly noteworthy is that on the northern, northeastern and eastern edges of such cloud, there are three roundish, nebulous extended regions, dominated by PAH emission as shown by their IRAC colours. Additional indication of warm-dust emission from them comes from the fact that they appear as shallow peaks of 70 μm emission, though not bright at longer wavelengths, in the *Herschel* maps (see Figs 1 and 3). Our narrow-band near-IR images (see left-hand panel of Fig. 13) indicate that the Brackett $\gamma$ emission of ionized gas is quite faint, as also indicated by the very faint emission in the 18 and 22.8 GHz continuum seen in Sánchez-Monge et al.'s (2013) maps. On the other hand, the diffuse broad $K_s$-band emission is dominated by light scattered by dust. Note also that these reflection nebulae contain a number of very red, embedded stars. In Section 3.3, we argued that our 2.2 μm star counts indicate overdensities in these small regions that we have labelled R1 and R2. Their sizes and the statistics of the star counts performed within their projected boundaries are listed in Table 4. Close-up images of the region are displayed in Fig. 13.

The IR photometry indicates that the stellar population embedded in these reflection nebulae is quite different in nature to that of the embedded cluster Cl 1 associated with core II (Section 3.3.1). R1 has a smaller number density of foreground stars ($H - K_s < 0.8$) compared to the entire studied area (Table 4). This implies that the local extinction in R1 is considerably higher than the mean $A_V$ determined for the whole region. In spite of this, we found that 22 out of a total of 30 (73 per cent) sources in R1 had $H - K_s > 0.8$ and are embedded in it. In contrast to Cl 1, their position in the $K_s$ versus $H - K_s$ diagram (Fig. 7) reveals no clearly defined pattern (e.g. an isochrone) that could suggest the existence of a young star cluster with a single age and extinction. The stars' magnitudes and colours are, rather, distributed almost uniformly over $\Delta K = 7$ and $\Delta(H - K_s) = 2$ magnitudes. More than 25 per cent of these stars show large IR excess emission, most probably originated in associated discs. They are marked by green arrows in Fig. 13 and their position and photometry is listed in Table 2.

The young stellar population that seems to be associated with the reflection nebula R2 appears somewhat more enigmatic. The dust extinction towards this area is similar to the mean for the whole

studied area, as the number density of foreground stars is similar to that expected statistically for homogeneous extinction (Table 4). The size of this nebula is significantly larger than that of R1 and the YSOs that appear to be related to it are much redder (corresponding to $A_V = 40$–55) than those of Cl 1 and R1. In fact, there is no single source in R2 with $H - K_s$ index between 0.8 and 2.0 (Fig. 7). This indicates that the dust cloud responsible for the local extinction has a sharp edge along the line of sight, and also suggests that several of the stars over a large area have significant IR-excesses (Table 2 and Figs 8 and 9). The most conspicuous of these objects are indicated by green arrows in Fig. 13. It is also important to note that the only small knot of $H_2$ 2.12 μm emission found in this survey is located just south of R2 and is indicated with a yellow arrow in the left-hand panel of Fig. 13. Likewise, the only (unresolved) small bright knot found to emit only in the 4.5 μm IRAC images is also located in the outskirts of R2. This object, with no counterpart in any other near- or mid-IR image, is indicated with a small circle in the left-hand and right-hand panels of Fig. 13. This could be a 'green fuzzy knot', thought to be due to molecular hydrogen emission lines in IRAC channel 2 bandpass (e.g. De Buizer & Bacca 2010). The very high extinction would make it undetectable in our narrow-band 2.12 μm image.

Finally, the presence of a smaller nebula (labelled N1 in Fig. 2) that is also a secondary 70 μm and PAH-dominated emission peak is located some 25 arcsec to the north-east of the centre of Cl 1. It appears to be an extension of the H II region G327.759-0.351, associated with core II. A single unresolved near- and mid-IR source with a large excess emission at $\lambda > 2$ μm is found within the small nebula and its position and photometry is listed in Table 2. Its location in the colour–magnitude diagram suggests a B0 spectral type with large $K$-band excess reddened by $A_V \simeq 40$.

### 3.4 IRAS 15507-I and the 'bar'

The dense core I is the less massive of the three cores found in the region. Near-IR source counts did not reveal any evidence of clustering. The surface number density of foreground stars in its vicinity is consistent with that expected for a uniform extinction across the studied area. As indicated by their photometry (Table 2),
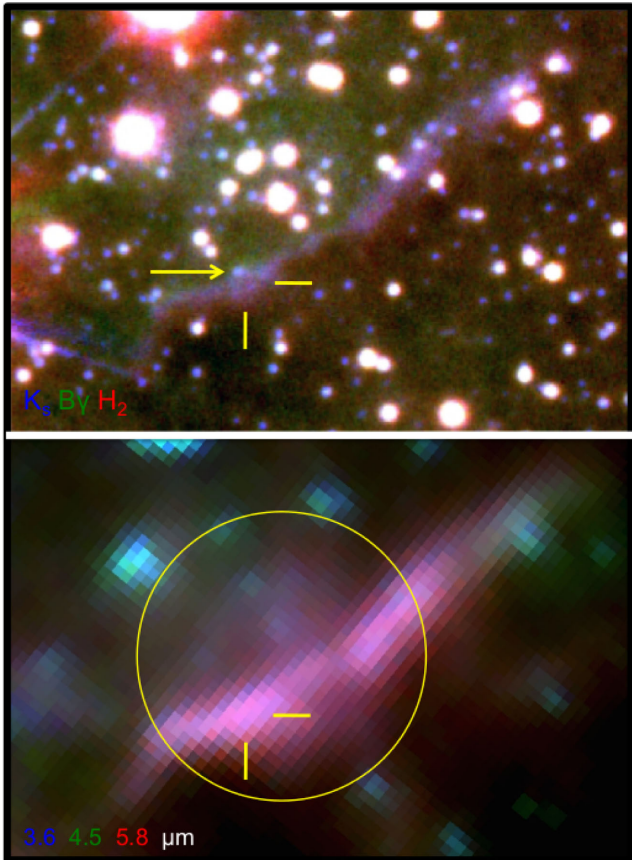
maximum is seen (marked in Fig. 14). Table 2 lists the photometry of this peak and its corresponding position in the IRAC two-colour diagram (Fig. 9) confirms its fluorescence-PAH line emission nature. A faint, very red near-IR source lies very close (marked with an arrow in Fig. 14) and tentatively, we may associate it with the extremely young object IRAS 15507-5359-I. With the combined near-IR, IRAC and *Herschel* SED of this source, shown in the left-hand panel of Fig. 11, we again used Robitaille et al.'s (2007) fitting engine to determine the range of physical parameters of the four models that best fit the core I SED. They are listed in Table 5. Although this exercise provides a good fit, one must bear in mind that the IRAC colours of this source are dominated by PAH emission lines and it is possible that the point-like near-IR source may not really be embedded in the bar and even be unrelated to core I. Still, we can speculate that this YSO is the prime responsible for ionizing the gas, creating a very diffuse, expanding, H II region.

## 4 CONCLUSIONS

The main conclusions of the morphological and photometric study of the star-forming region IRAS 15507-5359 in the wavelength range 1.2–500 μm are listed below.

(1) By analysing the distribution of the interstellar extinction along the line of sight, we confirmed that the distance to the complex is $5.0 \pm 0.5$ kpc.

(2) By way of *Herschel* mapping at 70, 160, 250, 350 and 500 μm, we found three dense cores separated by about 1 arcmin. Their masses range from 160 to almost 4000 $M_\odot$ and their mean temperatures from 16 to 25 K. The coolest and most massive one, core III, is a 'starless' infrared dark cloud with evidence of more recent star formation at its edges. Core II contains a rich, intermediate mass embedded cluster, Cl 1. Core I, the least massive one, seems to be associated with a high-luminosity Class I YSO and a large photodissociation front, though we found no evidence of an embedded stellar population.

(3) The embedded cluster, Cl 1, is composed of more than 45 young stars earlier than A0, approximately 15–20 per cent of them showing near-IR excesses. Its age is around one million years and it is reddened by more than 20 mag of visual extinction. The most massive young members of the cluster are responsible for ionizing the radio H II region G327.76-0.35. Close to its projected centre there is another, much younger, high-luminosity (3400 $L_\odot$) Class I YSO reddened by 25 mag of $A_V$.

(4) Though not showing the properties of developed clusters, we found two small zones in the outskirts of core III that is populated by aggregates of recently formed stars. These regions, R1 and R2, are surrounded by infrared reflection nebulae, PAH and 70 μm warm-dust emission. No isochrone or single $A_V$ could be defined for these two groups of embedded young stars. One of these regions, R2, contains the only shocked molecular hydrogen knot found in our survey.

(5) By fitting the 1.6 μm to 1.2 mm SEDs with Robitaille et al. (2006) models, we obtained the approximate physical properties of the central stars, accreting discs and envelopes of the two luminous Class I infrared YSOs. Their luminosities are a few thousand $L_\odot$ and their central star masses are around 10 $M_\odot$.

(6) IRAS 15507-5359 is another example of a massive cloud with distinct dense cores and embedded stellar populations, each in a different early evolutionary stage, with separations of around 1 pc.



**Figure 14.** Close-ups of the area containing the 'bar' associated with IRAS 15507-I. The $K_s$, Br $\gamma$ and H$_2$ composite (blue, green, red) image is shown in the upper panel and the IRAC 3.6, 4.5 and 5.8 μm image is shown in the lower panel. The centre of the circle corresponds to the position of the peak 260 μm emission (core I) and its size (19 arcsec) corresponds to that of the beam at that wavelength. The yellow arrow marks the very red star on the bar discussed in Section 3.4. The IRAC source listed in Table 2 that we associate with IRAS 15507-I is marked by two perpendicular yellow lines. Note that the width of the 'bar' is unresolved by *Spitzer*. In both, the centre is at $\alpha(2000) = 15^h54^m30.7$, $\delta(2000) = -54°08'03''$. Colour coding as in Fig. 13. North is to the top, east to the left.

the two brightest near- and mid-IR stars are in the foreground and, thus, unrelated to IRAS 15507-5359. Interestingly, as seen in the close-up IRAC and narrow-band images shown in Fig. 14, the far-IR peak emission coincides with a bright bar of emission with IRAC-bands colours that are typical of PAHs. Its length is approximately 40 arcsec and the position angle is 55°. Its width is unresolved by *Spitzer*. With the much higher spatial resolution of our near-IR narrow-band images (Fig. 14), a wiggled structure of the bar is evident in the $K_s$ band. The spectral structure of this bar resembles other photodissociation fronts seen in front of an expanding H II region (e.g. in the Orion nebula; Tielens et al. 1993) and other PDR fronts (e.g. Tapia et al. 2006). Across the bar, starting from the north-east to the south-west, we see the following pattern: extended and diffuse faint Br $\gamma$ emission ending abruptly at the bar that is delineated by a thin filament of 2.0–2.4 μm continuum followed by another similar one, dominated by faint H$_2$ line emission. This is consistent with the very faint extension of the radio-continuum emission (Sánchez-Monge et al. 2013). The peak 70–350 μm *Herschel* emission lies very close to the centre of the bar, where a compact PAH-emission

## ACKNOWLEDGEMENTS

## REFERENCES

Beltrán M. T., Brand J., Cesaroni R., Fontani F., Pesuto S., Molinari S., 2006, A&A, 447, 221
Benjamin R. A. et al., 2003, PASP, 115, 953
Bronfman L., Nyman L., May J., 1996, A&AS, 115, 81
Caswell J. L., Haynes R. F., 1987, A&A, 171, 261
Cesaroni R. et al., 2015, A&A, 579, A71
Churchwell E. et al., 2009, PASP, 121, 213
De Buizer J. M., Bacca W. D., 2010, AJ, 140, 196
Dutra C. M., Bica E., Soares J., Barbuy B., 2003, A&A, 400, 533
Elia D. et al., 2013, ApJ, 772, 45
Fazio G. et al., 2004, ApJS, 154, 10
Flaherty K. M., Pipher J. L., Megeath S. T., Winston E. M., Gutermuth R. A., Muzerolle J., Allen L. E., Fazio G. G., 2007, ApJ, 663, 1069
Giannini T. et al., 2012, A&A, 539, A156
Green J. A., McClure-Griffiths N. M., 2011, MNRAS, 417, 2500
Koornneef J., 1983, A&A, 128, 84
López-Chico T. A., Salas L., 2007, Rev. Mex. Astron. Astrofis., 43, 155
Lumsden S. L., Hoare M. G., Urquhart J. S., Oudmaijer R. D., Davies B., Mottram J. C., Cooper H. D. B., Moore T. J. T., 2013 ApJS, 208, 11
Marshall D. J., Robin A. C., Reylè C., Schultkeis M., Picaud S., 2006, A&A, 453, 635
Martini P., Persson S. E., Murphy D. C., Birk C., Shectman S. A., Gunnels S. M., Koch E., 2004, in Moorwood A. F. M., Masanori I., eds, Proc. SPIE Conf. Ser. Vol. 5492, Ground-based Instrumentation for Astronomy. SPIE, Bellingham, p. 1653
Molinari S. et al., 2010, A&A, 518, L100
Molinari S., Schisano E., Faustini F., Pestalozzi M., di Giorgio A. M., Liu S., 2011, A&A, 530, A133
Motte F. et al., 2010, A&A, 518, L77
Palla F., Brand J., Camoretto G., Felli M., Cesaroni R., 1991, A&A, 246, 249
Peretto N., Fuller J. A., 2009, A&A, 505, 405
Persson S. E., Murphy D. C., Krzeminski W., Roth M. Rieke M. J., 1998, AJ, 116, 247
Rieke G. H., Lebofsky M. J., 1985, ApJ, 288, 618
Robin A. C., Reylè C., Derrièr S. M., Picaud S., 2003, A&A, 409, 523, Erratum 2004, A&A, 416, 157
Robitaille T. P., Whitney B. A., Indebetouw R., Wood K., Denzmore P., 2006, ApJS, 167, 256
Robitaille T. P., Whitney B. A., Indebetouw R., Wood K., 2007, ApJS, 169, 328
Sánchez-Monge A., Beltrán M. T., Cesaroni R., Fontani F., Brand J., Molinari S., Testi L., Burton M., 2013, A&A, 550, A21
Schneider N. et al., 2012, A&A, 540, L11
Siess L., Dufour E., Forestini M., 2000, A&A, 358, 599
Skrutskie M. F. et al., 2006, AJ, 131, 1163
Slysh K. I., Kalenskii S. V., Valtss I. E., Otrupcek R., 1994, MNRAS, 268, 464
Stetson P. B., 1987, PASP, 99, 191
Tapia M., Persi P., Bohigas J., Roth M., Gómez M., 2006, MNRAS, 367, 513
Tapia M., Rodríguez L. F., Persi P., Roth M., Gómez M., 2009, AJ, 137, 4127
Tapia M., Persi P., Roth M., Elia D., Molinari S., Saldaño H. P., Gómez M., 2014, MNRAS, 437, 606
Tielens A. G. G. M., Meixner M. M., van der Werf P. P., Bregman J., Tauber J. A., Stutzki J., Rank D., 1993, Science, 262, 1986
Urquhart J. S. et al., 2013, MNRAS, 435, 400
Walsh A. J., Hyland A. R., Robinson G., Burton M. G., 1997, MNRAS, 291, 261
Werner M. et al., 2004, ApJS, 154, 1
Ybarra J., Tapia M., Román-Zúñiga C., Lada E., 2014, ApJ, 794, L25

This paper has been typeset from a TeX/LaTeX file prepared by the author.